Ultrafast X-ray CT imaging for hydrodynamic investigations of gas-liquid two-phase flow in centrifugal pumps

Schäfer, T.; Neumann-Kipping, M.; Bieberle, A.; Bieberle, M.; Hampel, U.;

Originally published:

November 2019

Journal of Fluids Engineering - Transactions of the ASME 142(2020)4, 041502

DOI: https://doi.org/10.1115/1.4045497

Ultrafast X-ray CT imaging for hydrodynamic investigations of gas-liquid two-phase flow in centrifugal pumps

Thomas Schäfer[a], Martin Neumann[a], André Bieberle[a,1], Martina Bieberle[a], Uwe Hampel[a,b]

[a] Helmholtz-Zentrum Dresden - Rossendorf, Institute of Fluid Dynamics,
Bautzner Landstr. 400, 01328 Dresden, Germany

[b] Chair of Imaging Techniques in Energy and Process Engineering,
Technische Universität Dresden, 01062 Dresden, Germany

[1] *Corresponding author. Tel.: +49-351-260-2913; fax: +49-351-260-2383*
E-mail address: a.bieberle@hzdr.de

Abstract

Gas entrainment into centrifugal pumps decreases pump performance and may raise safety issues, e.g. through insufficient cooling. Although there is some phenomenological knowledge in form of correlations between operating parameters and pump performance a further understanding via direct observation of the gas-liquid mixture was so far not possible. In this paper, we demonstrate the capability of ultrafast X-ray computed tomography (UFXCT) to disclose gas-liquid two-phase flow dynamics in the impeller region of a centrifugal pump mockup. Experiments were performed for gas injection at impeller speeds between 1300 rpm and 1600 rpm. We analyzed the time-resolved X-ray images with respect to the gas distribution and compared them with time-averaged image data of a real pump obtained earlier with gamma-ray tomography.

Keywords: centrifugal pump, gas-liquid two-phase flow, ultrafast X-ray computed tomography

1. Introduction

Centrifugal pumps are used in many industrial applications. They are economic and highly reliable, provide smooth and steady operation and offer low energy consumption. They are important primary components, e.g. in oil recovery plants to lift up crude oil to the surface and to convey it to petroleum production facilities [Barrios et al., 2011; Sabino et al., 2016; Bellary et al. 2018]. Furthermore, centrifugal pumps are also used in emergency cooling circuits of nuclear power plants [e.g.: Schultz et al, 2006; Stosic et al, 2008; Sato et al., 2009]. If water is taken there from reservoirs with free surfaces, the gas phase may undesirably become sucked into the pump. This reduces the flow rate of the pump and, thus, constitutes an important safety risk. To avoid and to handle such critical situations, it is necessary to investigate and understand the hydrodynamics of the two-phase flow inside centrifugal pumps. Furthermore, numerical fluid dynamics simulations may help in the future to improve centrifugal operations in their design. Hence, experimental data about two-phase flow in pumps is of high value.

Before starting with a review of the state of the art, relevant physical quantities for pumps in single and two-phase operation are introduced. A pump is characterized by its hydraulic power $P_{hyd} = Q_L \rho g h$ which is the power imparted by the pump on the fluid to increase its velocity and pressure. Q is the flow rate, ρ the fluid density, g is gravitational acceleration and h is the pump head. The pressure drop over the pump is Δp. For a gas-liquid flow we denote local cross-sectional values of gas holdup in the pump by the symbol α, while the inlet volumetric gas fraction is $\varepsilon = \frac{\dot{V}_G}{\dot{V}_L + \dot{V}_G}$ with $\dot{V}_G$ and $\dot{V}_L$ being the gas and liquid volumetric flow rates.

In 1974 Murakami et al. already investigated the behavior of entrained air bubbles and their effect on the pump performance distinguishing prime, head, discharge and efficiency. They investigated a radial semi-open impeller type pump and discovered that for smaller volumetric air entrainment ($\varepsilon \leq 0.04$) the performance reduces continuously with increasing ε whereas for higher air entrainment ($\varepsilon > 0.04$) the performance falls rapidly and discontinuities appear that change the flow pattern in the impeller abruptly. Furthermore, they developed and validated a theoretical approach for modeling the effects of the admitted air on the flow behavior and for calculating the performance curves under these two-phase flow conditions.

Thereafter, several other experimental and numerical studies have been conducted to investigate the performance of centrifugal pumps under varying operating conditions. In 1999, observations on a full-size nuclear reactor primary coolant pump operated at two-phase flow conditions have been reported by Chan et al. (1999). They disclosed the effects

of inlet flow temperature and initial flow conditions on the two-phase performance for very high gas entrainment (ε up to 0.40). In addition, Narabayashi et al. (1986) performed experiments using three scaled model pumps to examine the effects of specific pump speeds and characteristics of the high-void two-phase flow on the performance of centrifugal pumps in nuclear cooling circuits. The experimental analysis was accompanied by a data evaluation using the Transient Reactor Analysis Code (TRAC). They provided data, which are required to evaluate the primary loop recirculation (PLR) during a loss-of-coolant accident (LOCA). Pak et al. 1998 performed numerical analyses using three-dimensional finite volume method (FVM) to predict the flow characteristics of air-water two-phase turbulent flows in a centrifugal pump impeller and compared it with experimental data for additional gas phase, pressure and velocity in the impeller region. Here, the modeling of air-water two-phase mixture was proposed based on a bubbly flow model while the standard k-ε turbulence model was applied for the liquid phase only. Müller et al. 2015 evaluated the capability of the mono-dispersed multi-phase model in ANSYS CFX to predict the flow of liquid-gas mixture in radial pumps. In other studies, consequences of two-phase flow due to cavitation have been investigated [Duplaa et al., 2013; Tan et al., 2013; Coutier-Delgosha et al., 2003]. The study of Caridad et al. (2008) focused on the influence of bubble diameter and gas flow on the pump operation. Furthermore, Murakami et al., 1977 and Minemura et al., 1980, who theoretically and experimentally investigated the movement of entrained air bubbles with respect to the resulting change in pump performance, studied the physical behavior of one or few bubbles in an impeller. They also numerically calculated trajectories of isolated air bubbles in an impeller and compared it to experimental high-speed camera observations. In 2001, Amoresano et al. presented an experimental approach to characterize the two-phase flow field inside the impeller to understand the interaction between the gas and liquid phases under different inlet conditions. Therein, a correlation between gas-liquid structures and the energy dissipation phenomena in a centrifugal pump could be observed.

From the experimental side it is worth mentioning that conventional X-ray CT has already been applied to centrifugal pumps in the past, e.g. by Hassan et al. (2008). However, the spatial resolution was not sufficient which caused difficulties for quantitative code validation. High-speed videometry is another very popular and widely used method [Amoresano, et al., 2001; Barrios et al., 2011; Sabino et al., 2016]. However, its application needs an optical access to the flow as well as a low gas holdup.

Recently, our group has employed gamma-ray computed tomography (GammaCT) to study gas accumulations in an industrial centrifugal pump with a special approach, called time-averaged rotation-synchronized gamma-ray computed tomography [Bieberle et al., 2007]. The studies disclosed a gas accumulation in form of large gas pockets inside the impeller

chambers that is continuously increasing with the amount of gas entrainment [Schäfer et al., 2015; Neumann et al., 2016; Schäfer et al., 2017]. However, though gamma-ray imaging provides high resolution and very good phase fraction quantification [Bieberle et al., 2015] the reconstructed images contains only time-averaged information over approximately 600 s and hence no conclusions about the flow dynamics can be drawn.

Therefore, in this study we qualified ultrafast X-ray computed tomography (UFXCT) [Fischer et al., 2008] for dynamic studies of gas entrainment in an industrial-scale impeller mockup. This imaging technique has already been successfully applied for two-phase flow investigations in heated rod bundles [Barthel et al., 2013], structured packings [Janzen et al., 2013], ceramic foams [Zalucky et al., 2017a; Zalucky et al., 2017b], helical static mixers [Rabha et al., 2015], spout fluidized beds [Bieberle et al., 2016] and monoliths [Schäfer et al., 2016]. It allows contactless imaging of the two-phase distribution with high temporal and spatial resolution. However, since the penetration ability of X-rays is lower than that of gamma radiation, e.g. Cs^{137}, we must revert to a mock-up instead of an original industrial centrifugal pump. This mock-up comprises all the geometric features of an original pump but consists of lighter materials. With this mock-up, studies for different gas phase entrainment rates and with disperse and swirling gas-liquid inlet flow have been performed [Schäfer et al., 2019]. The corresponding two-phase flow in the impeller area has been scanned with a rate of 2,500 cross-sectional images per second. Additionally, the relative pressure at the suction side and the differential pressure across the pump were simultaneously recorded.

2. Materials

2.1 Experimental setup

The experimental setup for gas-liquid investigations in an impeller is shown in Figure 1a. It consists of a flow loop wherein a gas-liquid two-phase flow is continuously conveyed by the centrifugal pump mockup (Figure 1b). The impeller is made from polyamide and is manufactured by rapid prototyping technology. Its geometry is based on the original impeller geometry of an Etachrom BC 032-160/074 C11 (KSB) as earlier studies with gamma-ray CT were conducted at this type of pump [Schäfer et al., 2015, Neumann et al., 2016]. The most relevant geometric data are given in Table 1. The impeller design is shown in Figure 2. Furthermore, the entire CAD drawing data set is published by Schäfer et al. (2019).

A defined initial gas-liquid two-phase inlet flow is generated upstream of the impeller by a gas-liquid mixing module (see Figure 1a). In the experiments tap water and de-oiled pressurized air is used. The liquid is supplied from a 170 l reservoir, which also acts as a gas-liquid phase separator. The liquid temperature is controlled to 21 °C± 0.5 K during all

experiments. The liquid flow rate is measured upstream the mixing module by an inductive flow meter (MAG 1100, Siemens). The gas entrainment rate ε ($0 \leq \varepsilon < 1$) is continuously adjusted and the required gas flow rate Q_G is controlled by an air mass flow controller (FMA2600, Omega Newport), which is triggered by a programmable logic controller (SPS-ILC350ETH, Phoenix Contact) considering the current liquid flow rate Q_L according to

$$Q_G = \frac{\varepsilon}{1-\varepsilon} Q_L. \tag{1}$$

Furthermore, two different inlet two-phase flow regimes can be selected using a self-developed gas-liquid phase mixing module. These are dispersed bubbly two-phase flow and swirling two-phase flow with a stable gas core. Both flow regimes are typical for gas entrainment caused by hollow vortices [Hecker, 1981]. The flow loop is additionally instrumented with two pressure sensors to measure the relative pressure at the suction side (PXM419, Omega Newport) and the differential pressure across the pump (PD23, Omega Newport). The impeller itself is rotated by a driving shaft (see Figure 1b) that is again connected to a servomotor (ACA 90 S-4 / IE2, ecoDrives) that provides a selectable constant rotational speed between 1300 rpm and 1600 rpm. The final effective rotational speed is additionally directly measured using a Hall-effect sensor (GS105502, ZF Electronics), which is placed close to the driving shaft. This signal is later on used for exact image reconstruction of the rotating impeller.

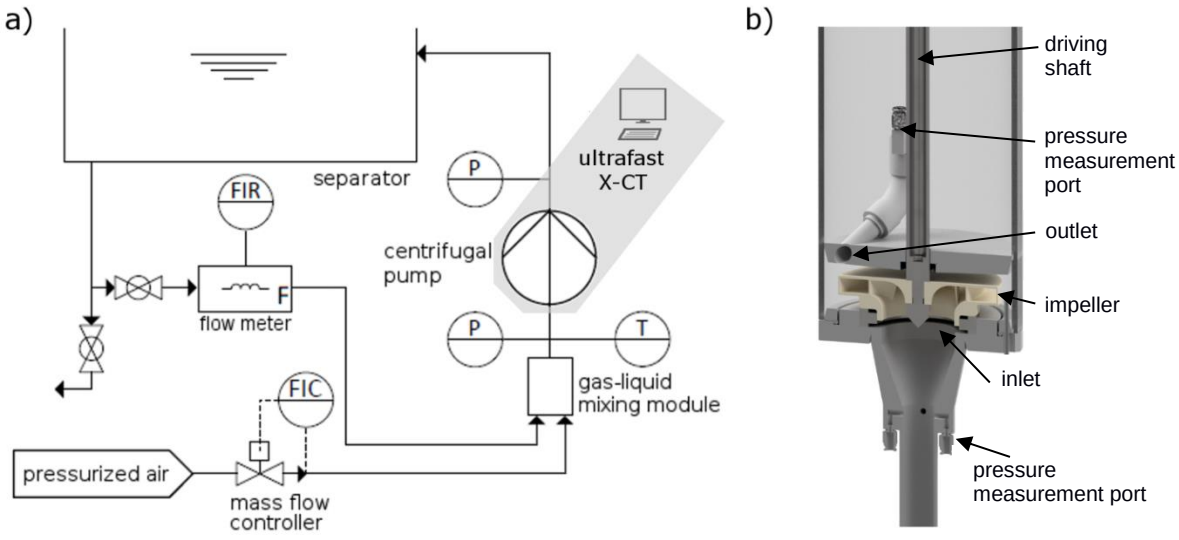

Figure 1: a) Schematic of the experimental setup and b) detailed view on the test section with the pump impeller.

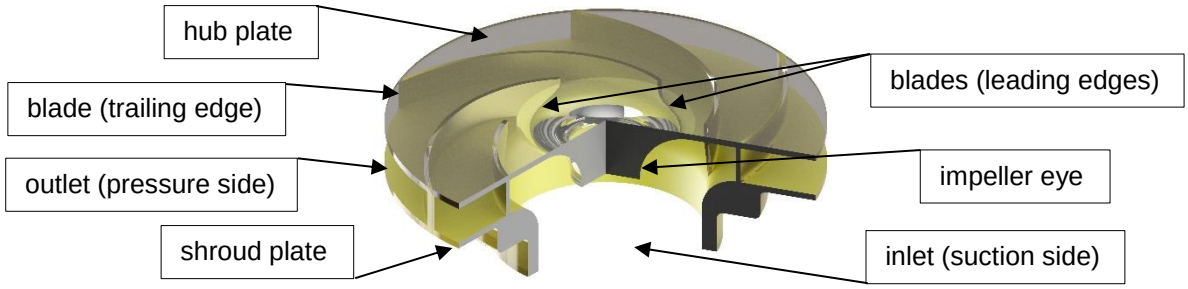

151

152 **Figure 2:** Semi-transparent visualization of the manufactured impeller.

153 **Table 1:** Geometric specifications of the impeller.

	property	value
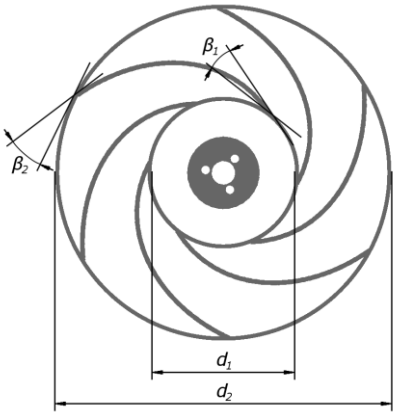	impeller inlet diameter d_1	54.0 mm
	impeller outlet diameter d_2	136.0 mm
	number of blades	6
	impeller inlet blade angle β_1	18.2°
	impeller outlet blade angle β_2	26.8°
	thickness of blades	2.0 mm
	chamber height (distance between hub plate and shroud plate)	12.0 mm
	impeller eye diameter (in the scanning plane)	32.0 mm

154

155 ## 2.2 Ultrafast X-ray CT imaging

156 Ultrafast X-ray computed tomography (UFXCT) has been applied to visualize the gas-liquid
157 phase distribution quantitatively inside the impeller region. The CT scanner comprises two
158 imaging planes with $N_d = 432$ detector elements each and is able to image objects up to
159 190 mm in diameter with an in-plane spatial resolution of about 1 mm. An imaging frequency
160 of $f^{(\mathrm{im})} = 2{,}500\,Hz$ (or frames per second) and single-plane scanning operation mode has
161 been selected for gas-liquid phase investigations in the rapidly rotating impeller area. For
162 image reconstruction, filtered back projection method is used [Hampel in Wang et al., 2015].

163 In contrast to conventional X-ray CT, in ultrafast X-ray CT the radiation source is artificially
164 rotated around the impeller mockup with the aforementioned frequency $f^{(\mathrm{im})}$ while projection
165 data is continuously acquired with a fixed frequency of $f^{(\mathrm{samp})} = 1\,\mathrm{MHz}$ using fixed
166 positioned radiation detector rings (see Figure 3). Thus, in total $N_p = 400$ projections are
167 obtained from the impeller that rotates during the CT scans with its own frequency $f^{(\mathrm{rot})}$.

Thus, additional data pre-processing must be performed to avoid motion blurring in the reconstructed images.

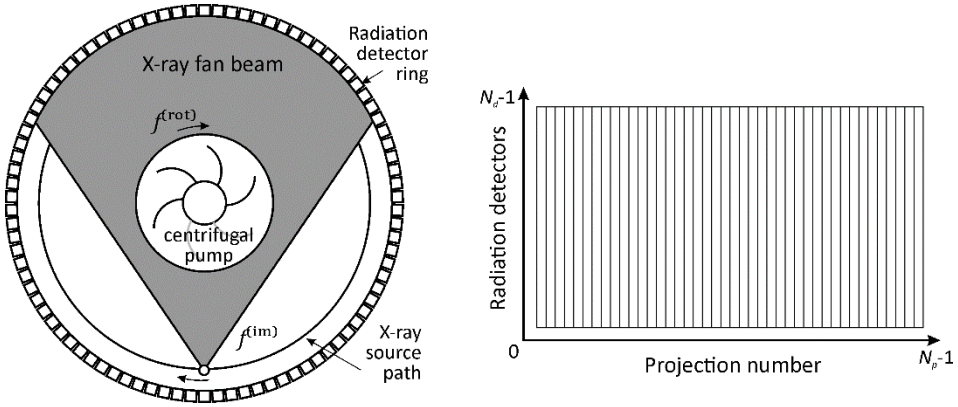

Figure 3: Sketch of ultrafast X-ray CT applied for investigation on rapidly rotating objects.

There are two ways to obtain image sequences for the rotating system. Either reconstruction is done in the fixed system and subsequently images are rotated or the projection data is shifted in the angular space according to the actual impeller angle, which is derived from the zero-crossing signal of the Hall sensor. The latter approach is to be preferred as interpolation is avoided. Assume we have a time interval $\Delta T^{(\mathrm{rot})}$ between two subsequent zero-crossing signals defining the time for one impeller revolution. Then, the impeller's angular progress within one image frame is

$$\Delta\varphi = 2\pi f^{(\mathrm{im})}\Delta T^{(\mathrm{rot})}. \tag{2}$$

Hence, the projection data has to be shifted by $N_p f^{(\mathrm{im})}\Delta T^{(\mathrm{rot})}$ angular samples to obtain an image in the rotating frame.

Another specific feature of the reconstruction procedure is that we account for the impeller rotation during the period where projection data for one image is acquired. Between two projections taken with $T^{(\mathrm{samp})} = 1/f^{(\mathrm{samp})} = 1\ \mu s$ temporal displacement the impeller moves a small angle of $2\pi T^{(\mathrm{samp})}/\Delta T^{(\mathrm{rot})}$. This angular displacement is encountered by another data shift during reconstruction and thus, rotational fluctuations and drifts are compensated which guarantees cross-sectional images with no motion blurring.

2.3 Determination of local gas holdup and gas-liquid interface

Result of image reconstruction is a stack of images whose pixels contain the local X-ray attenuation values $\mu_{i,j,k}^{(\mathrm{rec})}$. Thereby i and j denote the spatial pixel index and k the image number within the temporal sequence. The reconstructed linear attenuation coefficient is typically prone to errors coming from beam hardening, radiation scattering but also slight electron beam misalignments. Therefore, we normalize the values with the help of average gray values from image regions with known linear attenuation. Such are the average attenuation coefficient $\bar{\mu}^{(\mathrm{P})}$ of the acrylic pump casing and $\bar{\mu}^{(\mathrm{G})}$ the average attenuation coefficient of the "gas-filled" pixels outside the pump (see Figure 4). With that, the normalization is given as

$$\mu_{i,j,k} = \frac{\mu_{i,j,k}^{(\mathrm{rec})} - \bar{\mu}^{(\mathrm{G})}}{\bar{\mu}^{(\mathrm{P})} - \bar{\mu}^{(\mathrm{G})}}. \tag{3}$$

From this, we compute the gas holdup values $\alpha_{i,j,k}$ from the attenuation data according to

$$\alpha_{i,j,k} = 1 - \frac{\mu_{i,j,k}^{(\mathrm{TP})}}{\overline{\mu}_{i,j}^{(\mathrm{L})}}, \tag{4}$$

where $\mu_{i,j,k}^{()}$ represents the CT data sets obtained at gas-liquid two-phase flow (TP) and liquid single-phase flow (L), respectively.

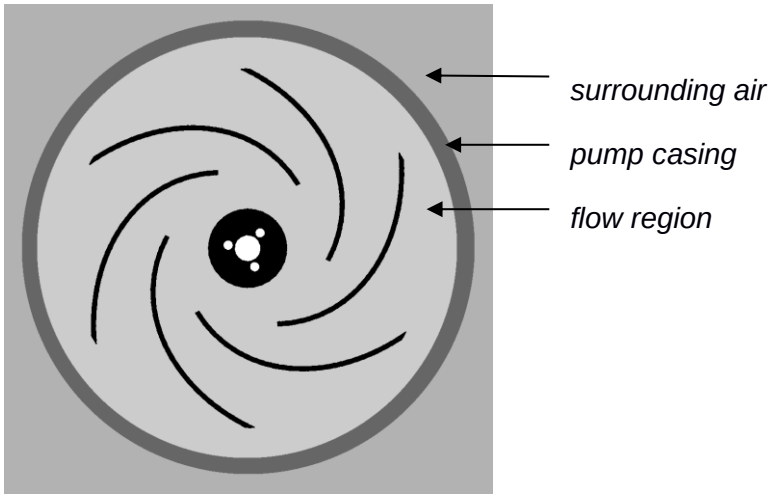

Figure 4: Schematic of material distribution within the reconstructed cross-sectional images used for image improvement.

Note, with reference to the color bars in the figures below that due to noise in the reconstructed images the calculated gas holdup may statistically deviate from its mean value. This may lead to unphysical local phase fraction values outside the range [0,1]. Usually, data is cut to the physical minimal or maximal value. However, as this occurs errors in calculation of space and time averaged holdups those values are left as they are.

For the extraction of the gas interface, an algorithm firstly published by Li et al. (2011) and adapted for two-phase flow interface extraction in Sohr et al. (2019) has been applied. The algorithm is based on the level set method with application to image segmentation and considers intensity inhomogeneity within the image, which may occur in X-ray CT imaging due to scattering and beam hardening. The resulting gas interface can be divided into gas-liquid (free) and gas-solid (bounded by the impeller structure) interface sections. To distinguish both of them, the mask of the impeller is applied. An interface length parameter, which is corresponding to interfacial area, is then calculated as the sum of distances between neighboring contour points, i.e. the length of a piecewise linear approximation of the contour, which, however, is only an approximation on a sub-pixel scale. In Figure 5 a representative illustration of a cross-sectional gas holdup image with indicated gas-liquid (red) and gas-solid interface (green) is shown.

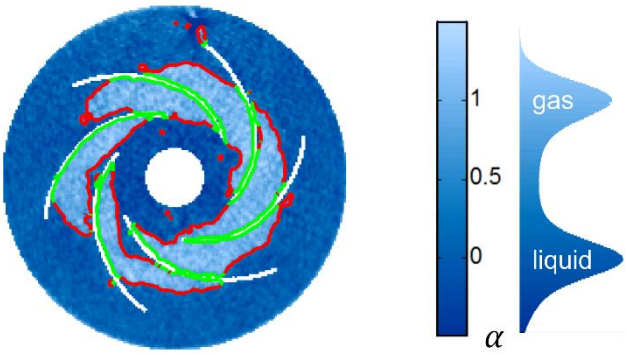

Figure 5: Cross-sectional gas holdup image with indicated gas-liquid (red) and gas-solid interface (green).

2.4 Experimental procedure

The experimental procedure described next has been performed for all experimental points, that is, 117 operating points in total (for the full experimental data set see Schäfer et al. (2019)). However, in this paper only an exemplary data set at 1480 rpm impeller speed,

dispersed gas phase injection and different gas flow rates is used for discussion. Initially, the rotational speed of the impeller is set to constant nominal rotational speed of 1480 rpm. Subsequently, disperse gas entrainment (bubbly two-phase flow) is adjusted and varied in discrete steps of $\Delta\varepsilon = 0.002$ in the range from $\varepsilon = 0.008$ to $\varepsilon = 0.058$. The latter corresponds to the maximum value prior to severe performance drop.

The corresponding performance curves, that is for liquid conveying rate Q_L, differential pressure Δp across the pump and relative hydraulic power $P_{\mathrm{hyd,rel}}$

$$P_{\mathrm{hyd,rel}}(\varepsilon) = \frac{P_{\mathrm{hyd}}(\varepsilon)}{P_{\mathrm{hyd}}(\varepsilon = 0)} = \frac{Q_L(\varepsilon) \cdot \Delta p(\varepsilon)}{Q_L(\varepsilon = 0) \cdot \Delta p(\varepsilon = 0)} \tag{5}$$

are shown in Figure 6.

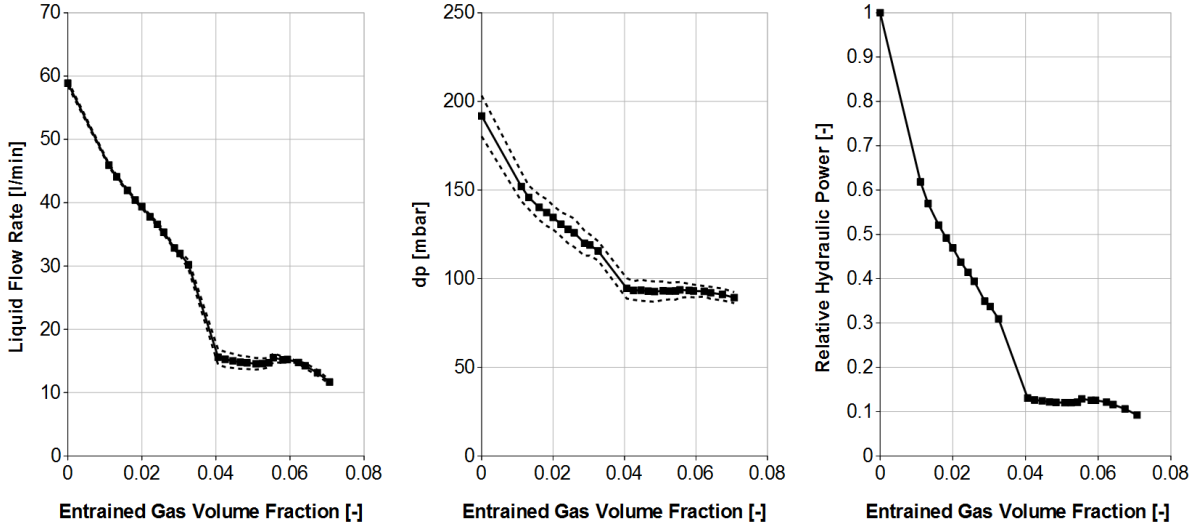

Figure 6: Performance curves of the investigated centrifugal pump mockup.

Prior to the experiments, for each gas entrainment value, the conveyance curve is checked for stability over the time, to be sure that the pumping system is operated in steady-state condition. Subsequently, UFXCT scanning is performed for an interval of 5 s, which gives $K = 12{,}500$ cross-sectional images of the impeller. The residual temporal fluctuations of the liquid flow rate and the differential pressure during the tomographic scans have been found to be between ±0.46 % and ±7.86 % (relative to mean liquid flow rate) and ±3.19 % and ±6.36 % (relative to mean differential pressure), respectively and are represented as dashed lines in the corresponding diagrams in Figure 6.

3. Results

3.1 Comparison with gamma-ray CT measurements

Initially, the function of the impeller mockup and, therefore, the transient behavior of the two-phase fraction distribution have been evaluated to conform to the already existing tomographic images obtained from the original industrial pump [Schäfer et al., 2015], where gamma-ray CT scans provided single time-averaged (600 s) but angle-resolved images of the two-phase distribution. Therefore, the three corresponding UFXCT scans have been temporally averaged (5 s) over all K images. As can be seen in Figure 7 the comparison yields a strong agreement, with minor differences in the overall gas holdups $\bar{\alpha}$ originate (beside others) that may occur from slightly different applied impeller area mask sizes.

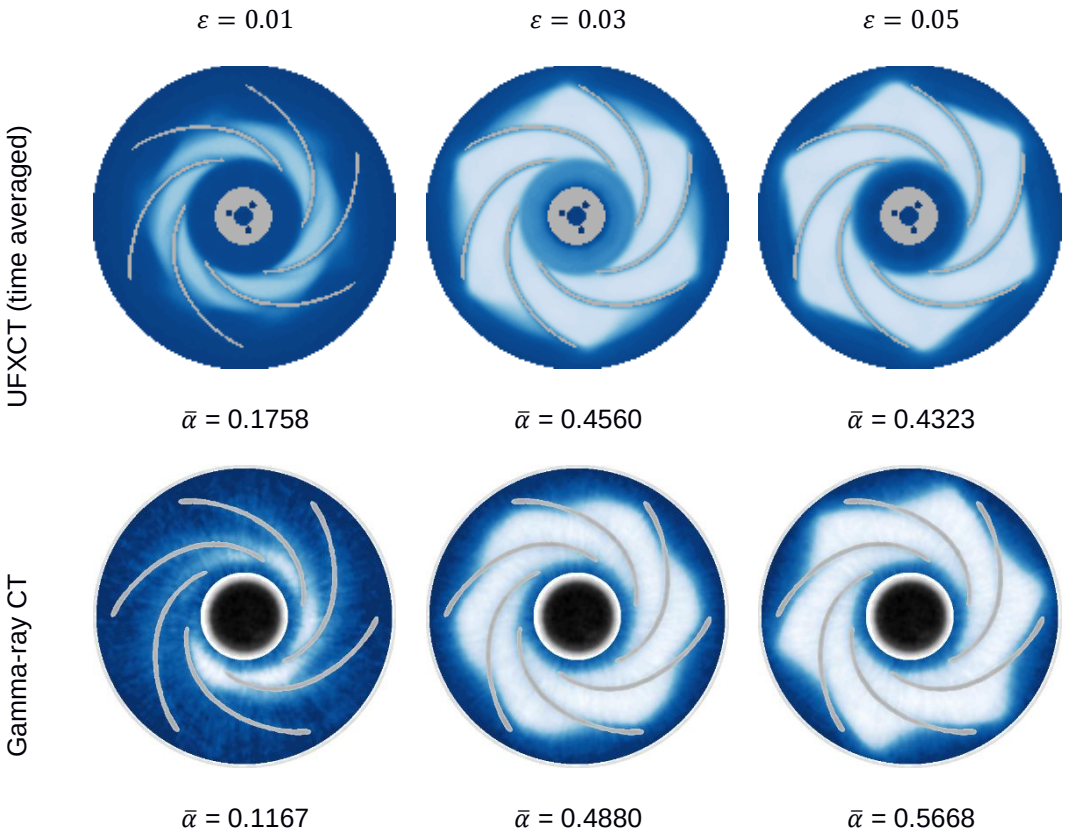

Figure 7: Comparison of selected cross-sectional and time-averaged gas holdup distributions in a rotating impeller at 1480 rpm using UFXCT and gamma-ray CT [Schäfer et al., 2015] technique. The gas phase is injected in dispersed form.

3.2 Qualitative analysis

In Figure 8, a selection of the obtained instantaneous UFXCT tomographic images is shown. Furthermore, the corresponding image sequences (image sequences 1-6) are provided as supplementary material to this publication. They provide an impression of the way certain gas-liquid structures form out in the heavily agitated mixture. For example, small lamella-like structures of pure liquid are observable at the pressure side of the blades from time to time. Here, liquid is shooting through the accumulated gas pockets in short-term surges. This is observed especially for lower gas entrainment. Furthermore, at higher gas entrainment, large bubbles are temporally visible in the area of the impeller eye. These bubble agglomerations are stable in position and shape for a certain time. Since they are upstream of the inlets of the impeller chambers, they indicate liquid transport blockage at these positions. In the area of the chamber outlets gas detachment is observed. Here, small gas bubbles are detached from the accumulated gas pockets. In the impeller outlet areas, protruding gas plumes have been detected for higher gas entrainment ($\varepsilon \geq 0.03$). These gas plumes are growing out of the chambers along the suction sides of the blades into the flow area outside the impeller.

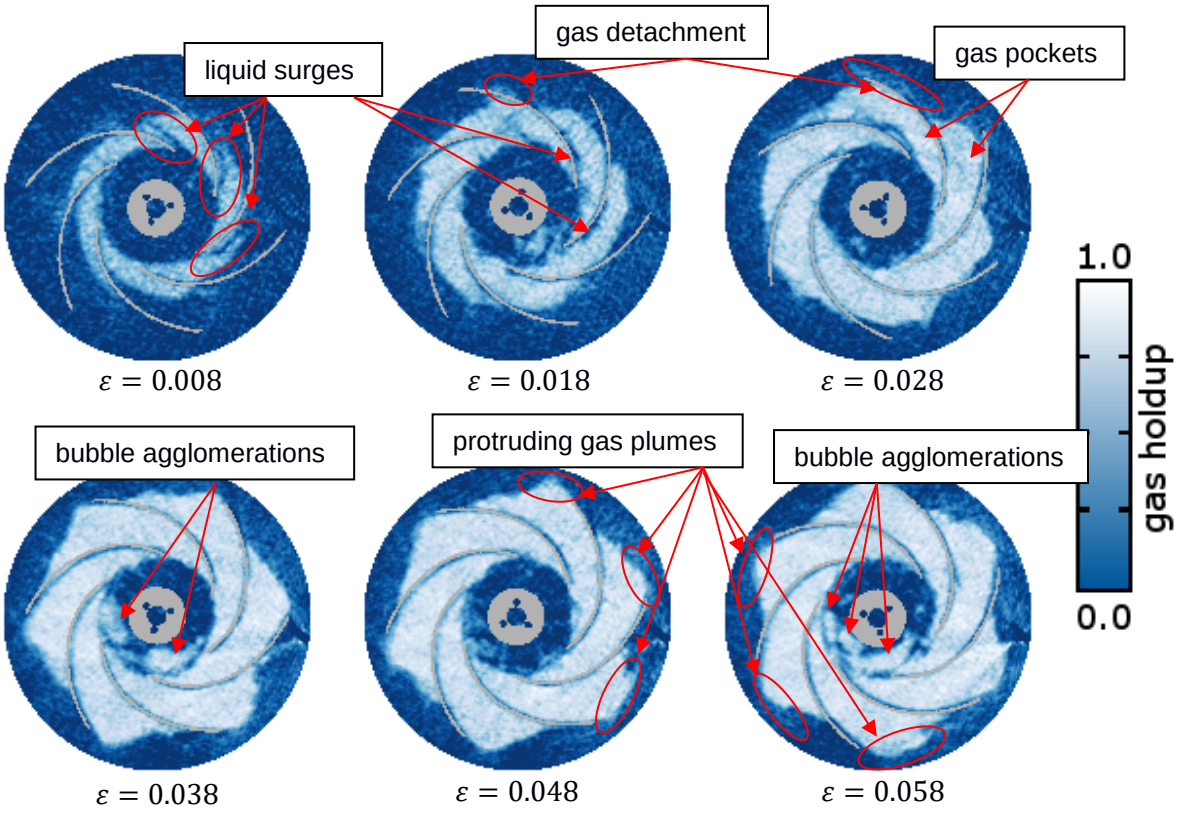

Figure 8: Characteristic gas-liquid flow patterns inside the impeller under increasing gas entrainment conditions and at 1480 rpm.

3.3 Quantitative analysis of the image sequences

From the gas holdup images, gas interfaces and their length (corresponding to interfacial area) are determined. A selection of images with the extracted gas-liquid interface is shown in Figure 9. As can be seen, relevant structures including small bubbles and thin liquid surges are captured. Especially the latter are clearly distinguished from gas-solid interfaces with no liquid in between.

A quantitative analysis of the gas-liquid interface (Figure 10) reveals different trends of gas-liquid and liquid-solid interface. While the gas-solid interface correlates with injected gas flow rate, the free gas-liquid interface remains nearly constant in the considered cases.

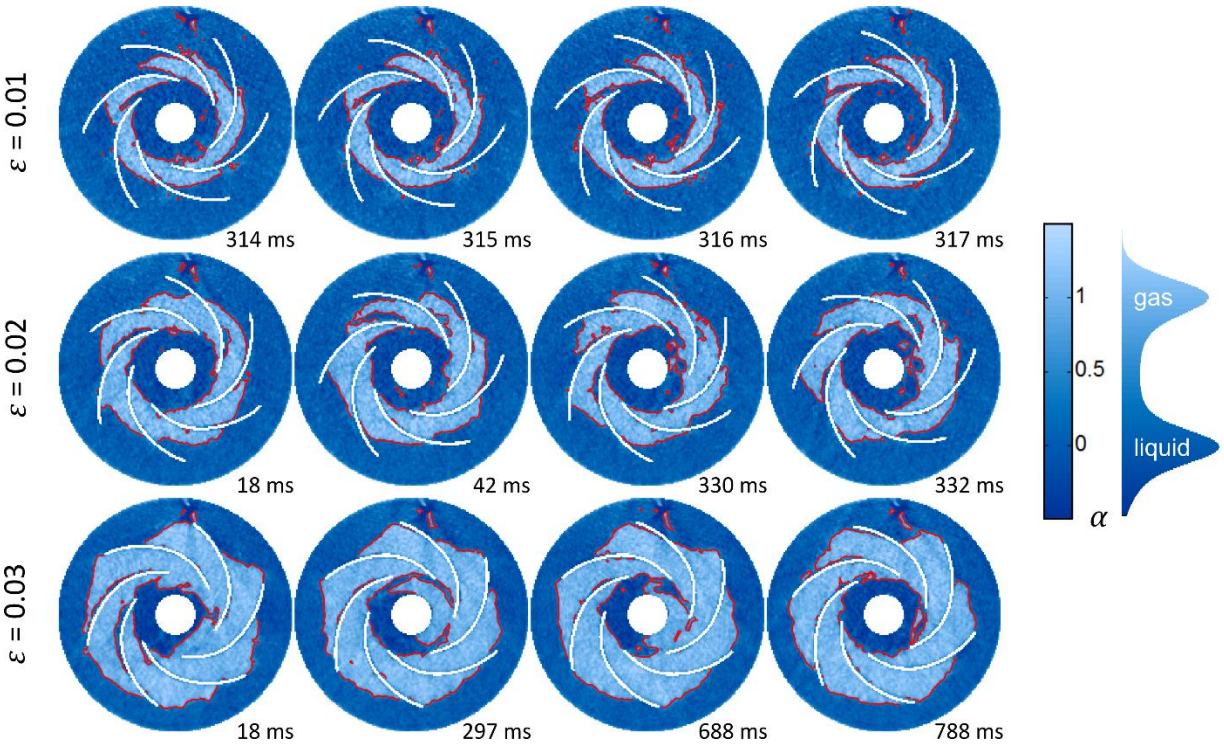

Figure 9: Extracted gas-liquid interface (indicated in red) for three inlet gas entrainments at different points in acquisition time.

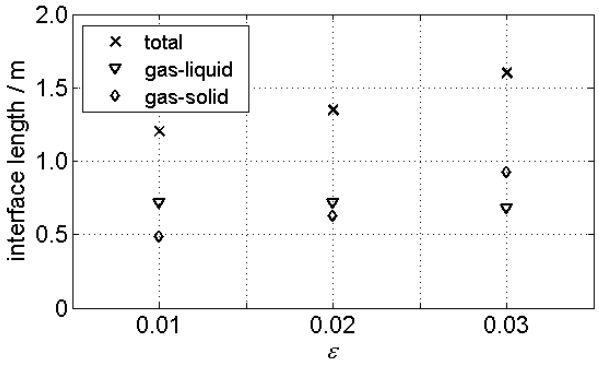

300

301 **Figure 10:** Averaged length of the gas interface within the cross-section divided into the gas-liquid
302 interface and gas-solid interface.

303

304 Taking the obtained tomographic images and selecting only the flow area of one impeller
305 chamber gives a detailed view on the accumulated gas pockets and the gas-liquid interfaces
306 (Figure 11 A-O). Looking at the images qualitatively, different shapes of the accumulated gas
307 pockets are clearly visible. Furthermore, areas with temporal changing phases can be
308 discovered. That is, intensive phase interactions between liquid and gas pockets occur.
309 Furthermore, a temporal shifting of the gas pockets, especially at the suction side of the
310 blades can be observed. This indicates pressure fluctuations and corresponding forces
311 acting on the liquid phase and gas phase. In addition, temporal fluctuations of the local
312 pressure field inside the chambers, which may lead to compression and decompression of
313 the gas pockets, is observed.

314 For quantitative analysis, the temporal gas holdup inside single chambers are calculated of
315 each reconstructed cross-sectional image for three different gas entrainments. Figure 11
316 shows the graphs of temporal progression of gas holdup inside a selected chamber. The
317 spatial distribution and development of the gas and liquid is visualized using tomographic
318 images that are assigned to the graphs and selected time steps. Considerable periodic gas
319 holdup fluctuations can be observed, especially for the case of gas entrainment of 0.03.
320 Here, the areas of gas and liquid are rapidly moving inside the chamber, which again trigger
321 the intensive phase interactions.

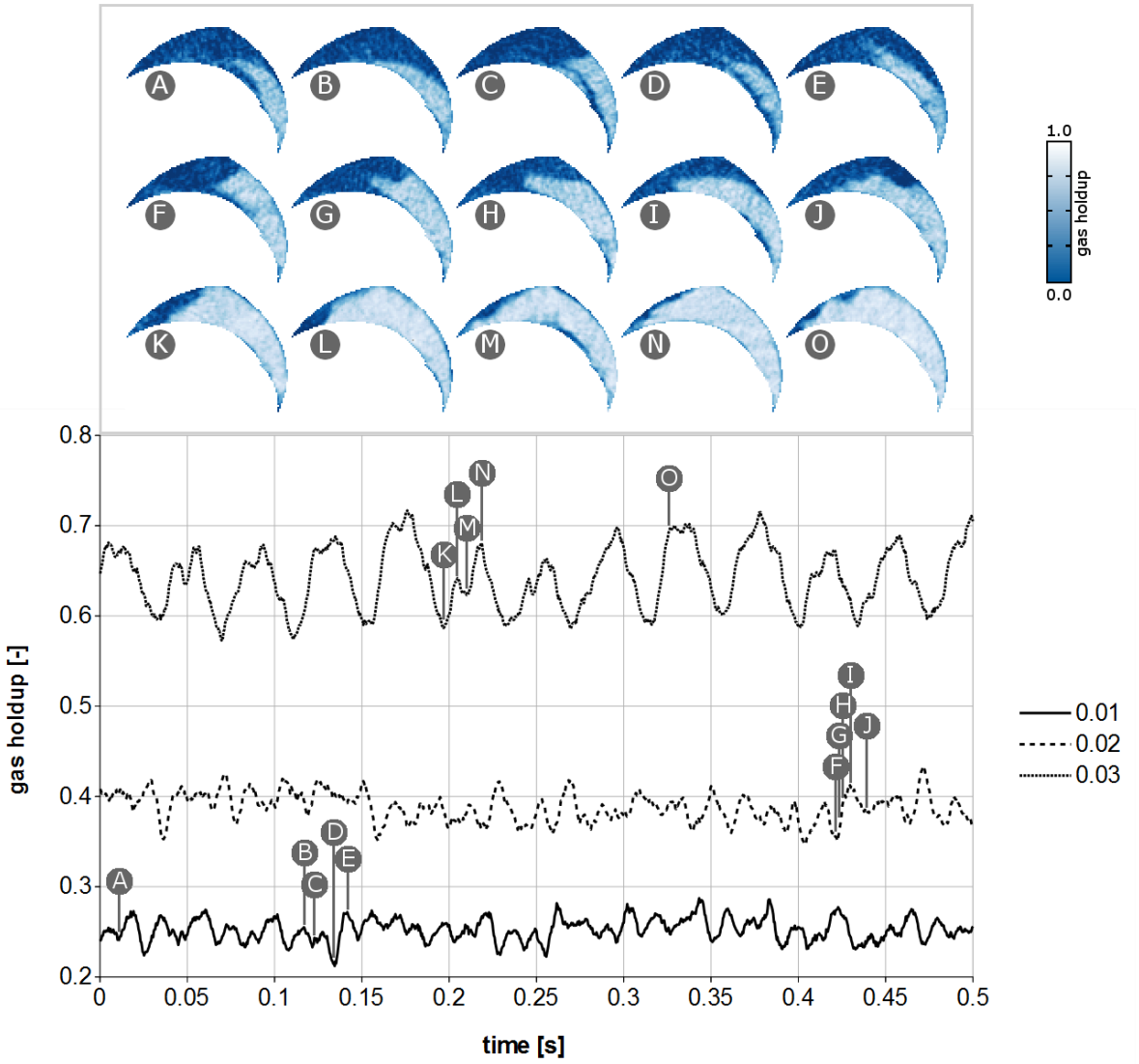

322

323 **Figure 11:** Gas holdup evolution inside a single chamber of the impeller for different gas flow rates
324 and corresponding tomographic images of selected states.

325

326 Eventually, the standard deviation

$$\sigma_{i,j} = \frac{1}{K-1} \cdot \sum_{k=1}^{K} \left(\alpha_{i,j,k} - \bar{\alpha}_{i,j}\right)^2 \tag{6}$$

327 of the cross-sectional gas holdup can be used as a measure of the equiprobability of phases
328 in a volume element over time, which has been visualized in Figure 12 for various gas
329 entrainments. That is, it indicates areas with frequent phase transition. Such areas are
330 mainly found at the inlets of the chambers, the pressure sides of the blades or the wake of
331 the gas pockets. In contrast, a high stability of the gas pockets inside the chambers,

especially at the suction side of the blades, can be observed. Additionally, a very high interaction rate occurs in the area of the impeller eye at gas entrainments of $\varepsilon = 0.03$ and $\varepsilon = 0.04$. This results from the large and unsteady gas agglomerations, which have been observed in the impeller eye and have been described before.

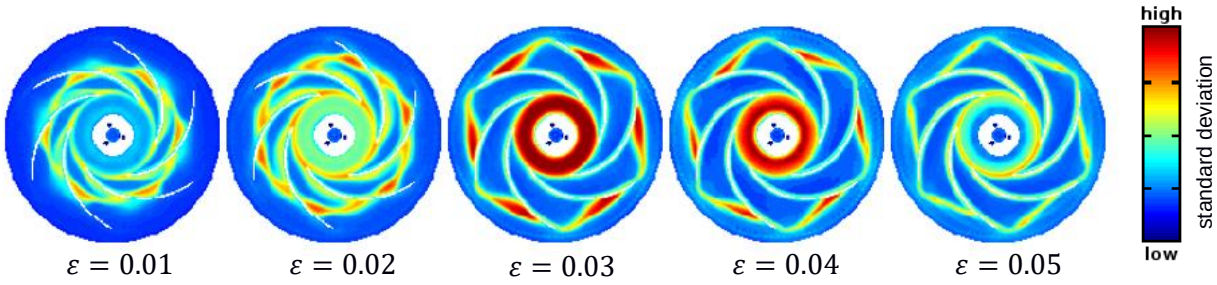

Figure 12: Visualization of the standard deviation of the cross-sectional gas holdup.

4. Conclusion

In this paper, the capability of ultrafast X-ray computed tomography to disclose transient gas-liquid flow behavior within a centrifugal pump has been demonstrated. With the presented setup, cross-sectional gas phase distribution image sequences have been recorded for two general gas inlet conditions (disperse and swirling), three rotational speeds and inlet gas fraction in the range between 0.008 and 0.058. The fast imaging discloses the dynamics of even small flow structures very well. This includes gas bubbles of various size and thin liquid surges. Analysis of interfacial area and gas holdup variability showed, that gas-liquid interfaces in the impeller eye and in the chambers towards the outlet are highly agitated but also that the gas plugs in the chambers are very stable and hinder the transport of liquid. A more detailed analysis of this rich data is an upcoming task.

Acknowledgment

The project was founded by the German Federal Ministry of Education and Research (BMBF) under the funding code 02NUK023B.

References

Amoresano, A.; Langella, G.; Noviello, C. Experimental analysis of air bubble inside a centrifugal pump. *Transactions on Modelling and Simulation* Vol. 30 (**2001**) pp. 23-32.

Barrios, L; Prado, M.G. Experimental visualization of two-phase flow inside an electrical submersible pump stage. *Journal of Energy Resources Technology* Vol. 133 (**2011**) pp. 042901/1-042901/12. doi: 10.1115/1.4004966.

Barthel, F.; Franz, R.; Hampel, U. Experimental investigations of single and two-phase flow in a heated rod bundle. *Kerntechnik* 78 (1) (**2013**) pp. 60-67. doi: 10.3139/124.110316.

Bellary, S.A.I.; Husain, A.; Samad, A.; Kanai, R.A. Performance Optimization of Centrifugal Pump for Crude Oil Delivery. *The Journal of Engineering Research* Vol. 15 (1) (**2018**) pp. 88-101. doi: 10.24200/tjer.vol15iss1pp88-101.

Bieberle, A.; Schleicher, E.; Hampel, U. Data acquisition system for angle synchronized gamma-ray tomography of rapidly rotating objects. *Measurement Science and Technology* 18 (11) (**2007**) pp. 3384-3390. doi:10.1088/0957-0233/18/11/018.

Bieberle, A.; Schäfer, T.; Neumann, M.; Hampel, U. Validation of high-resolution gamma-ray computed tomography for quantitative gas holdup measurements in centrifugal pumps, *Measurement Science and Technology* 26 (**2015**) pp.1-12. doi:10.1088/0957-0233/26/9/095304.

Bieberle, M; Barthel, F. Combined phase distribution and particle velocity measurement in spout fluidized beds by ultrafast X-ray computed tomography. *Chemical Engineering Journal* 285 (**2016**) pp. 218–227. doi: 10.1016/j.cej.2015.10.003.

Caridad, J.; Asuaje, M.; Kenyery, F.; Tremante, A.; Aguillón, O. Characterization of a centrifugal pump impeller under two-phase flow conditions. *Journal of Petroleum Science and Engineering* 63 (1-4) (**2008**) pp. 18-22. doi: 10.1016/j.petrol.2008.06.005.

Chan, A.M.C.; Kawaji, M.; Nakamura, H.; Kuikita, Y. Experimental study of two-phase pump performance using full size nuclear reactor pump. *Nuclear Engineering and Design* 193 (**1999**) pp. 159-172. doi: 10.1016/S0029-5493(99)00150-8.

Coutier-Delgosha, O.; Fortes-Patella, R.; Rebound, J.L.; Hofmann, M.; Stoffel, B. Experimental and numerical studies in a centrifugal pump with two-dimensional curved blades in cavitating condition. *Journal of Fluids Engineering* 125 (**2003**) pp. 970-977. doi: 10.1115/1.1596238.

Duplaa, S.; Coutier-Delgosha, O.; Dazin, A.; Bois, G. X-Ray measurements in a cavitating centrifugal pump during fast start-ups. *Journal of Fluids Engineering* 135 (**2013**) pp. 041204/1-041204/9. doi: 10.1115/1.4023677.

Fischer, F.; Hoppe, D.; Schleicher, E.; Mattausch, G.; Flaske, H.; Bartel, R.; Hampel, U. An ultra fast electron beam x-ray tomography scanner. *Measurement Science and Technology* 19 (9) (**2008**) 094002. doi: 10.1088/0957-0233/19/9/094002.

Hampel, U.; Image reconstruction for hard field tomography, in: Mi Wang: Industrial Tomography: Systems and Applications, Amsterdam: Woodhead Publishing, 2015, 1782421181, 347-376.

Hassan W.; Legoupil, S.; Chambellan, D.; Barre, S. Dynamic localization of vapor fraction in turbo pump inducers by X-ray tomography. *IEEE Transactions on Nuclear Science* Vol. 55 (1) (**2008**) pp.656-661. doi: 10.1109/TNS.2007.914023.

Hecker, G.E. Model-prototype comparison of free surface vortices. *Journal of the Hydraulics Division ASCE* 107 (**1981**) pp. 1243-1259.

Janzen, A.; Schubert, M.; Barthel, F.; Hampel, U.; Kenig, E.Y. Investigation of dynamic liquid distribution and hold-up in structured packings using ultrafast electron beam X-ray tomography. *Chemical Engineering and Processing: Process Intensification* 66 (**2013**) pp. 20-26. doi: 10.1016/j.cep.2013.01.008.

Li, C.; Huang, R.; Ding, Z.; Gatenby, J.C.; Metaxas, D.N.; Gore, J.C. A Level Set Method for Image Segmentation in the Presence of Intensity Inhomogeneities With Application to MRI, *IEEE Transactions Image Processing* 20 (**2011**) 2007–2016. doi: 10.1109/TIP.2011.2146190.

Minemura, K.; Murakami, M. A theoretical study on air bubble motion in a centrifugal pump impeller. *Journal of Fluids Engineering* Vol. 102 (**1980**) pp. 446-453. doi: 10.1115/1.3240721.

Müller, T.; Limbach, P., Skoda, R. Numerical 3D RANS simulation of gas-liquid flow a centrifugal pump with an Euler-Euler two-phase model and a dispersed phase distribution. *Proceedings of 11th European Conference on Turbomachinery Fluid Dynamics and Thermodynamics ETC11* Madrid Spain March 23-27 (**2015**).

Murakami, M.; Minemura, K. Effects of entrained air on the performance of a centrifugal pump - 1st report. *Bulletin of the JSME* Vol. 17 (110) (**1974a**) pp. 1047-1055. doi: 10.1299/jsme1958.17.1047.

Murakami, M.; Minemura, K. Effects of entrained air on the performance of a centrifugal pump – 2nd report. *Bulletin of the JSME* Vol. 17 (112) (**1974b**) pp. 1286-1295. doi: 10.1299/jsme1958.17.1286.

Murakami, M.; Minemura, K. Flow of air bubbles in centrifugal impellers and its effects on the pump performance. *Proceedings of the 6th Australian Hydraulics and Fluid Mechanics Conference* Adelaide Australia December 5-9 (**1977**).

Narabayashi, T.; Arai, K.; Kubokoya, T.; Amano, O.; Gomyo, T. Centrifugal pump behavior in steady and transient two-phase flow. *Journal of Nuclear Science and Technology* 23 (2) (**1986**) pp. 136-150. doi: 10.3327/jnst.23.136.

Neumann, M.; Schäfer, T.; Bieberle, A.; Hampel, U. An experimental study on the gas entrainment in horizontally and vertically installed centrifugal pumps. *Journal of Fluids Engineering* Vol. 138 (09130) (**2016**) pp. 1-9. doi: 10.1115/1.4033029.

Pak, E.T.; Lee, J.C. Performance and pressure distribution changes in a centrifugal pump under two-phase flow. *Proc. Inst. Mech. Eng.* 212 (**1998**) pp. 165-171. doi: 10.1243/0957650981536835.

Rabha, S.; Schubert, M.; Grugel, F.; Banowski, M.; Hampel, U. Visualization and quantitative analysis of dispersive mixing by a helical static mixer in upward co-current gas-liquid flow. *Chemical Engineering Journal* 262 (**2015**) pp. 527-540. doi: 10.1016/j.cej.2014.09.019.

Sabino, R.H.G.; Stel, H.; Bertoldi, D.; Morales, R.E.M. Theoretical-experimental analysis of two-phase flow in an electrical submersible pump impeller. *Proceedings of 9th International Conference on Multiphase Flow ICMF-2016* Firenze Italy May 22-27 (**2016**).

Sato, T., Akinaga, M., Kojima, Y., Two types of a passive safety containment for a near future BWR with active and passive safety systems, Nuclear Engineering and Design 239 (2009) 1682–1692

Schäfer, T.; Bieberle, A.; Neumann, M.; Hampel, U. Application of gamma-ray computed tomography for the analysis of gas holdup distributions in centrifugal pumps. *Flow Measurement and Instrumentation* 46 (**2015**) pp. 262-267. doi: 10.1016/j.flowmeasinst.2015.06.001.

Schäfer, T.; Meitzner, C.; Lange, R.; Hampel, U. A study of two-phase flow in monoliths using ultrafast single-slice X-ray computed tomography. *International Journal of Multiphase Flow* 86 (**2016**), pp.56–66. doi: 10.1016/j.ijmultiphaseflow.2016.07.008.

Schäfer, T.; Neumann, M.; Bieberle, A.; Hampel, U. Experimental investigations on a common centrifugal pump operating under gas entrainment conditions. *Nuclear Engineering and Design* 316 (**2017**) pp. 1–8. doi: 10.1016/j.nucengdes.2017.02.035.

Schäfer, Thomas, Bieberle, André, Pietruske, Heiko, & Hampel, Uwe. (2019). Ultrafast X-ray tomography data set for the investigation of gas-liquid two-phase flows in an impeller of a centrifugal pump [Data set]. Rodare. http://doi.org/10.14278/rodare.76

T.L. Schulz, Westinghouse AP1000 advanced passive plant, Nuclear Engineering and Design 236 (2006) 1547-1557.

Sohr, J.; Bieberle, M.; George, G. R.; Flechsig, S.; Kenig, E. Y.; Schubert, M.; Hampel, U. Comparative assessment of different image processing methods to determine the gas-liquid interfacial area in froth regimes of sandwich packings from ultrafast X-ray tomography image data. *Chemical Engineering Research and Design* (2019) (accepted).

Stosic, Z.V., Brettschuh, W., Stoll, U., 2008. Boiling water reactor with innovative safety concept: The Generation III+ SWR-1000. Nucl. Eng. Des. 238, 1863–1901. doi:10.1016/j.nucengdes.2007.12.014

Tan, L.; Zhu, B.S.; Cao, S.L.; Wang, Y.M. Cavitation flow simulation for a centrifugal pump at low flow rate. *Chinese Science Bulletin* 58 (8) (**2013**) pp. 949-952. doi: 10.1007/s11434-013-5672-y.

Zalucky, J.; Wagner, M.; Schubert, M.; Lange, R.; Hampel, U. Hydrodynamics of descending gas-liquid flows in solid foams: Liquid holdup, multiphase pressure drop and radial dispersion. *Chemical Engineering Science* 168 (**2017a**) pp. 480–494. doi: 10.1016/j.ces.2017.05.011.

Zalucky, J.; Claußnitzer, T.; Schubert, M.; Lange, R.; Hampel, U. Pulse flow in solid foam packed reactors: Analysis of morphology and key characteristics. *Chemical Engineering Science* 307 (**2017b**) pp. 339–352. doi: 10.1016/j.cej.2016.08.091.